Metallurgical and Materials Engineering *Research paper*
Association of Metallurgical Engineers of Serbia AMES *https://doi.org/10.30544/809*

SIMULTANEOUS IMPROVEMENT OF CORROSION AND MECHANICAL PROPERTIES OF AA 5083 ALUMINUM ALLOY

Q. Tayyaba[1], A.Q. Butt[1], M. Shahzad[1], T. Ali[2]*

[1] Materials Division, Pakistan Institute of Nuclear Science and Technology, Nilore, 45650, Pakistan
[2] Physics Division, Pakistan Institute of Nuclear Science and Technology, Nilore, 45650, Pakistan

Received 10.11.2021

Accepted 17.06.2022

Abstract

In this study, the effects of cold-rolling and annealing on the structural, electrochemical, and mechanical properties of AA5083 in a simulated seawater environment are investigated. The results demonstrated that annealing temperature significantly affects the alloy's mechanical and corrosion properties. According to potentiodynamic results, the rate of corrosion decreased after annealing. Compared to the cold-rolled sample, the heat treatment doubles the electrochemical impedance, indicating that the corrosion resistance of AA5083 alloy is suitable at 50°C annealing. Approximately twice as much ductility was added to the materials as compared to the as-received materials. Additionally, the mechanical testing revealed the Portevin-Le Chatelier (PLC) Effect Type B band, which reflected the smaller grain size.

Keywords: aluminum alloy; annealing; mechanical properties; corrosion behavior.

1. Introduction

Aluminum-magnesium alloys are widely used in naval shipbuilding, cryogenic vessels, automotive body structures, trains, and many other metal products due to their higher strength-to-weight ratio, improved corrosion resistance, and excellent mechanical properties [1-3]. Corrosion resistance of aluminum alloys is linked to the protective oxide film that forms on the alloy's surface under normal atmospheric conditions [4, 5].

Aluminum-magnesium alloys (5xxx series) are non-heat treatable alloys [6] and contain Mg as the primary alloying element, which improves the mechanical and corrosion properties through work hardening and solid solution strengthening [7]. The electrode potential of β-phase (Mg_2Al_3) is lower than that of the aluminum matrix, which reduces corrosion resistances as it precipitates continuously along the grain

* Corresponding author: Qanita Tayyaba, *qanita750@yahoo.com*

boundaries at 50-200 °C and appears to be corroded in corrosive environments due to anodic reactions [8-10]. To prevent intergranular precipitation, exfoliation, and stress corrosion cracking caused by the continuous accumulation of β-phase along the grain boundaries, the maximum solubility of Mg in aluminum at room temperature is 6 % by weight [11]. There is no grain boundary phase in the microstructure of AA5083, but there are intermetallic precipitates (Mg, Mn, Fe,Si) or (Mg, Si) in Al-Mg solid solution [12-14].

These intermetallic precipitates create inhomogeneities on the surface of AA5083 alloy, making it susceptible to localized corrosion in an environment containing sea water [15, 16]. When exposed to high temperatures in sea water (particularly Cl^- ion), the resulting oxide film can degrade at specific points and form pits. Due to the presence of magnesium as an alloying element, the application of these alloys is limited at high temperatures. [17,18]. In the case of AA5083, the higher magnesium content restricts the working temperature of these alloys to below 65°C prior to cold working (cold rolling) and various "H" tempers [19]. After cold working at room temperature, the alloy ages and softens, but eventually reaches a stable state. Typically, this is accomplished by a thermal stabilization procedure as the final step in the production of H32 or H321 tempers. AA5083 can be annealed by heating to 345°C, maintaining a uniform temperature, and then cooling; the rate of cooling is insignificant. Numerous studies have investigated the effect of annealing temperature on microstructure and mechanical properties [20-22]; additionally, the corrosion behavior of annealed Al-Mg alloys micro-alloyed with certain elements has been investigated by electrochemical method in a 3.5% NaCl solution [23]. Different authors have investigated the impact of annealing temperature on the susceptibility to stress corrosion cracking [24, 25].

Due to the ever-increasing number of marine-applicable structures, it is crucial to examine the behavior of these materials (5xxx series). In marine water, these materials are subject to the combined effects of stress and corrosion. Therefore, sheets of AA-5083 that had been subjected to a standard treatment cycle (H32) were utilized, and the annealing conditions for these sheets were optimized to produce the best results in the simulated maritime environment. The current study investigates the effect of cold rolling and annealing on the electrochemical behavior of AA5083 alloy in simulated seawater using potentiodynamic polarization and electrochemical impedance spectroscopy, as well as the effects of stress corrosion cracking, which must be taken into account for the cumulative action of stresses and corrosion. Optical and scanning electron microscopy was used to examine the microstructure and fractographic features of annealed samples exposed to simulated seawater for electrochemical and stress corrosion cracking investigations. Consequently, the purpose of this research is to enhance the pre-processing conditions for Al-Mg alloys in order to improve the corrosion resistance and mechanical properties, thereby extending the service life of structures made from this alloy.

2. Experimental procedure

The AA5083 billets received were rolled and treated according to the condition H32, i.e., strain hardened, and then stabilized to a strain hardening of approximately 25 % [26]. After achieving the required hardness for H32, different types of testing were conducted based on the marine applications of these alloys [27]. These tests include corrosion studies, mechanical characterization, and slow strain rate testing to evaluate

the stress corrosion crack behavior of the alloy in a marine environment. In order to examine the impact of the marine environment, samples were tested in a simulated marine environment.

2.1 Materials and Metallography

The chemical composition of the Al-Mg alloy used in this study, as determined by ICP-OES (iCAP 6500 series Thermoscientific) analysis, is presented in Table 1, and Fig. 1. depicts the XRD pattern of annealed samples obtained using Cu K radiation (= 0.154 nm) with a step size and step time of 0.05 and 1.0, respectively, and a scan range of 70 angstroms.

Table 1. Chemical Composition of AA5083 Alloy.

Elements	Mg	Mn	Cr	Ti	Fe	Si	Cu	Zn	Al
Concentration (%)	4.35	0.53	0.15	0.02	0.57	0.14	0.02	0.02	Balance

2.2 Electrochemical corrosion testing

The corrosion behavior of cold-rolled and annealed AA5083 alloy in seawater (3.5 % NaCl) solution was evaluated through DC polarization (Tafel analysis) using Gamry Reference 600 and standard graphite rod as counter electrodes and Ag/AgCl as the reference electrode. Before beginning the experiment, the samples were stabilized at their open circuit potential (OCP) for 30 minutes. At a scan rate of 1 mV/s, Tafel Plots were determined from -0.25 V to +0.25 V with respect to open-circuit potential. The corrosion potentials (Ecorr.), corrosion current densities (iCorr.), anodic Tafel slopes (a), and cathodic Tafel slopes (c) were extracted from the potentiodynamic polarization plots using Tafel extrapolation techniques.

Mechanical Testing

Before and after 50°C annealing, AA5083 sheets were characterized mechanically under different conditions, namely before and after annealing. The AA5083 undergoes tensile testing and micro-vicker hardness testing as part of its mechanical testing. Sub-sized samples with a 30-mm gauge length and a 6-mm gauge diameter underwent tensile testing. The examination was conducted in accordance with ASTM standard B557 at a strain rate of 0.003 s-1. Prior to annealing, the isometric behavior of H32 AA5083 was validated using samples prepared in both the rolling and transverse directions in order to compare the effect of direction on the mechanical properties of AA5083. After annealing, tensile tests were also conducted on H32-treated AA5083. The samples were annealed at a mean temperature of 500°C for 30 minutes, and their tensile test results were compared to those of samples without heat treatment.

Vickers hardness testing was performed on H32-treated AA5083 using a machine of Model DMH-2 with a load of 25 gf and a dwell time of 15s to measure the surface hardness. The results of hardness tests performed on AA5083 before and after annealing were compared to determine the effect of heat treatment on the hardness of these alloys.

Stress corrosion cracking (SCC) analysis was the final phase of material characterization for H32-treated AA5083. Before and after annealing, SCC tests were

conducted to determine the effect of heat treatment on the performance of these alloys in marine water conditions. The SCC tests were conducted using a strain rate on the order of 10-6/s in the presence of a simulated marine environment at an elevated temperature.

3. Results & Discussion

3.1 Microstructure Analysis:

Optical microstructure of as-received, cold-rolled, and annealed sample is depicted in Figure 1. Figure 1. (a) depicts the as-received structure consisting of variously shaped grains with a nominal diameter of 193 µm and a homogeneous equiaxed grains microstructure. Figure 1. (b) depicts the cold-rolled state with elongated and fibrous grains in the rolling direction and parallel bands of elongated substructures measuring 0.5-.10 µm in length and 0.08-0.1 µm in width. Figure 1. (c) demonstrates that annealing treatment modifies the grain morphology; second-phase particles tend to precipitate along the grain boundaries appearing dark range up to about 2–3 µm in size in microstructure, which was also confirmed by the low-intensity peaks of XRD, with roughly equiaxed grains size ranges of 35 µm to 85 µm and relatively uniform grain size after annealing at 50°C.

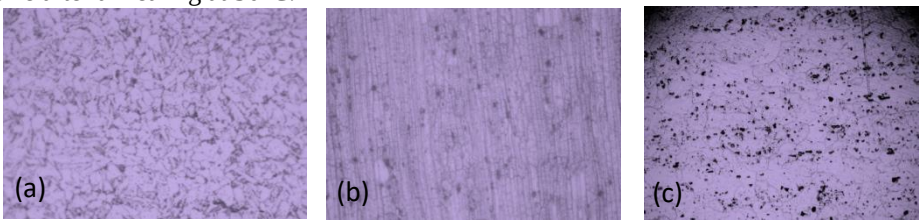

Fig. 1. Optical microscopy of AA5083 Alloy (a) as-received (b) cold rolled (c) annealed.

3.2 XRD Results

Figure 2. depicts the X-ray Diffraction patterns of as-received, cold-rolled, and annealed samples. Table 2. displays the calculated values of lattice parameter a, crystallite size D, and lattice strain calculated from broadening of X-ray diffraction peaks by taking into account the full width at half maximum (FWHM) of the individual peaks. The AA5083 alloy displays four strong and sharp 2 peaks centered at 38.4, 44.6, 65.1, and 78.2°, which correspond to the (111), (200), (220), and (311) planes, indicating the absence of impurities. The peak Al (Fe, Mn) phase after annealing at angles 2theta 14° and 22° corresponds to (100) and (101). The weak peaks are identified as Al (Fe, Mn) phases based on crystallographic data reported in the scientific literature. Extremely weak peaks indicate that the observed peaks are typically associated with small volume fractions of these phases in the bulk material [30]. According to the scientific literature, the preferred orientation of the crystal may influence the peak height in a particular plane. It is possible that the effects of annealing on the material account for the lower peak intensity after heat treatment. According to reports, annealing reduces stress or increases crystallite size, both of which result in an increase in peak intensities or peak height [28, 30]. The crystallographic arrangement changes as grains rotate to achieve an easy plane, and the changes in peak intensity are related to

the increase in crystallite size caused by annealing, atomic rearrangement, and stress relief [29-31].

The X-ray patterns of as-received, cold-rolled, and heat-treated α-Al samples are indicative of the FCC crystal structure (JCPDS No. 89-4037). The sample lattice parameters, as shown in Table 2, are in good agreement with the published values for the α-phase Aluminum FCC structure: a = 4.047 ± 0.01 nm [28,31]. The Scherrer equation [32] was utilized to determine crystallite size and lattice strain from the broadening of X-ray diffraction peaks, which can be represented as

$$D\ (crystallite) = \frac{k\lambda}{\beta cos\theta} \qquad 1$$

and

$$\varepsilon\ (strain) = \frac{\beta}{4tan\theta} \qquad 2$$

where λ is the wavelength of the X-rays used, β is full width half maximum (FWHM) of diffraction peak, θ is the Bragg angle, D is the average crystallite size measured in a direction perpendicular to the surface of the specimen, and k is a constant (k = 0.9).

The calculated average crystallite size of the particles increased from 47.9 nm to 74.34 nm during the annealing process, while the average lattice-strain decreased to its minimum value of 3.43 x 10-3. This behavior can be explained by the preferential grain direction resulting from the rolling direction and sheet production route. Due to the conditions of annealing, grain growth becomes random after annealing. This is due to the reduced stresses in annealed samples. The increase in crystalline size results in a substantial improvement in their corrosion resistance. Increasing the lattice parameter alters the mechanical properties of the material.

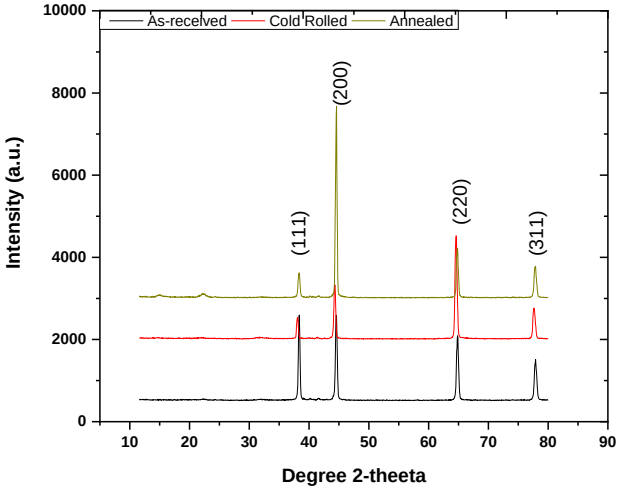

Fig. 2. XRD pattern of AA5083 alloy annealed at different temperatures.

Table 2. Calculated values of lattice parameter, crystallite size, Lattice Strain with Standard Deviation (SD) of AA5083 before and after Heat treatment at different temperatures.

Annealing Temperatures	Lattice Parameter a (nm) ± SD	Crystallite Size D (nm) ± SD	Lattice Strain ($\varepsilon*10^{-3}$) ± SD
As-received	0.432 ± 0.02	47.91 ± 2.20	2.54 ± 0.08
Cold Rolled	0.435 ± 0.03	52.04 ± 2.10	3.65 ± 0.07
Annealed	0.436 ± 0.02	74.34 ± 2.20	3.43 ± 0.04

3.3 Potentiodynamic polarization test

3.3.1 Potentiodynamics results

Figure 3. depicts the potentiodynamic polarization curves of Cold-rolled (CR) and annealed alloy (AS) in a 3.5% solution of seawater. Table 3. provides a summary of the electrochemical parameters extracted from the potentiodynamic polarization curves. The results indicate that annealing followed by cold rolling in a 3.5% NaCl medium reduces the corrosion rate. For annealed samples, the corrosion potential shifts to the positive side, indicating that the anodic process is significantly more affected than the cathodic process. The greater electropositive corrosion potential (Ecorr) indicates that annealed samples are more resistant to corrosion. Tafel plots reveal that the annealed alloy has a higher electropositive corrosion potential value (0.90 V vs Ag/AgCl), whereas the value for the corrosion rate (CR) is approximately -0.96, indicating an increase in corrosion rate and a corresponding decrease in passivity for CR. The corrosion current density (icorr) of the annealed alloy is lower (0.554 μA·cm−2) than that of the cold rolled specimen (1.530 μA·cm−2). Consequently, the corrosion current density of the annealed sample is approximately 100 times less than that of the cold-rolled alloy, and it has a higher corrosion resistance. This minimal shift in the corrosion potential (relative to SCE) suggests that the protective layer (aluminum oxide) acted by merely blocking the surface's reaction sites without affecting the anodic and cathodic reaction mechanisms. The corrosion resistance follows the same trend observed in electrochemical impedance studies, according to the findings of polarization studies. This corrosion rate was derived directly from Gamry Echem Analyst utilizing the in-built Tafel fitting.

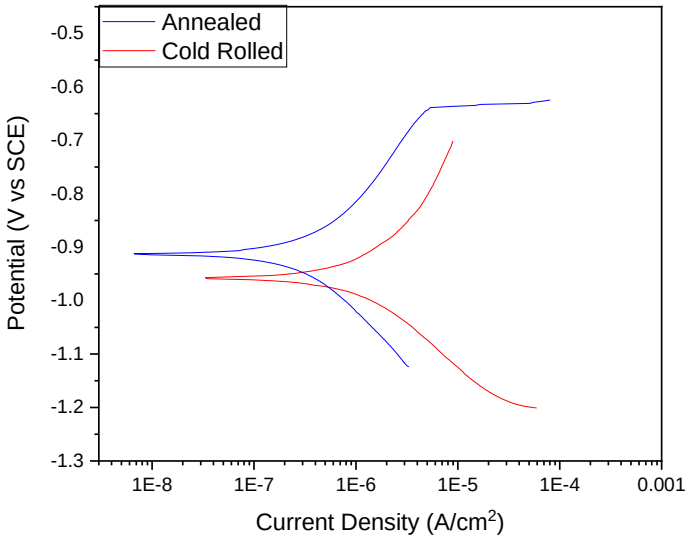

Fig. 3. Tafel curves (a) cold rolled (b) 50 °C annealed.

Table 3. Corrosion Rate of AA5083 alloy at Different Temperatures.

Samples	Beta A (V/decade)	Beta C (V/decade)	Icorr (nA)	Ecorr (mV)	Corrosion Rate (mpy)
Cold Rolled	308.5e-3			-958.0	397.0e-3
		193.2e-3	1.530 µA		
Annealed	288.4e-3	285.8e-3	554.0	-913.0	144.1e-3

3.3.2 Electrochemical Impedance Spectroscopy

Figure 4. depicts the EIS spectra in the form of a Nyquist curve for the cold rolled (CR) and annealed (AS) Al-based alloy in a 3.5% NaCl solution. The experimental findings are consistent with the electrical equivalent circuit model depicted in Figure 5. The Nyquist plot for CR and AS samples at RT demonstrates identical behavior; however, the capacitive semicircle for CR samples is larger than that of AS samples.

For both samples, the circuit shown in Fig. 4. is used to describe the substrate/solution interface model usually known as the Randle's model. The parameters calculated from these models have been given in Table 4. In this circuit, Ru is the solution resistance, Rp is charge transfer resistance, CPE is constant phase element. The impedance behavior of CPE can be stated as

$$Z_{CPE} = \left(Y_o \, R_p^{1-a}\right)^{1/a} \qquad 3$$

where, Yo is the CPE constant (in Ω−1·sn·cm-2) and a is the phase shift, which can be used as a gauge of the inhomogeneity or roughness of the surface.

At high frequencies, the electrochemical impedance results indicate the presence of a capacitive loop (HF). Polarization resistance is a measure of a metal's resistance to

corrosion in a particular environment; it decreases as temperature rises. In Nyquist curves, the diameter of the semicircle represents charge transfer resistance R_{ct} equal to polarization resistance R_p. In addition, the diameter of the semicircle in the Nyquist curves is larger for AS samples, indicating a greater polarization resistance. The polarization resistance increases from 30.25e3 Ω to 43.29e3Ω and the capacitance parameter Y_o increased from 18.64e-6 to 24.07e-6 $S.s^n$, when the cold rolled sample is annealed. This shows that the electron transfer for the metallic materials is slower by annealing; also illustrating that higher polarization resistance Rp mean better corrosion resistance and a lower corrosion rate.

The parameter *a* is a measure of the deviation from ideal capacitive behavior and represents the dispersion power of CPE which is between 0 and 1. When a = 1, the CPE behaves as an ideal capacitor, and a < 1, due to inhomogeneities in the substrate system, such as porosity, roughness or non-uniform current distribution [33].

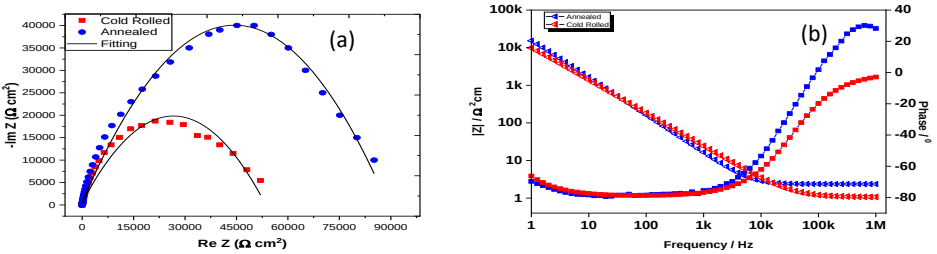

Fig. 4. Nyquist & bode plots of cold rolled and annealed alloy in the 3.5% NaCl solution along with fit data based on the models shown in Fig. 5.

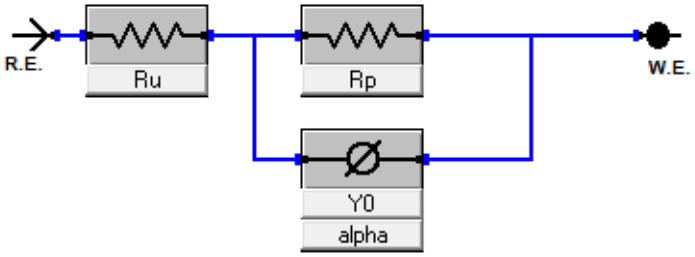

Fig. 5. The equivalent circuit models for EIS data fitting.

Table 4. Fitting Results of Electrical Elements for Cold Rolled Alloy and 50°C Annealed.

Samples	Ru (Ω)	Y_o ($S.s^n$)	a	R_p (Ω)
Cold Rolled	1.061	18.64e-6	8.812e-1	30.25e3
Annealed	2.173	24.07e-6	8.899e-1	43.29e3

In the Bode plot displayed in Fig. 4, log Z and θ are plotted against log f. Since frequency appears as one of the axes in the Bode plot, it is simple to deduce from the plot that impedance is dependent on frequency. The log |Z| versus log curve can be utilized to calculate Rp and Ru. At extremely high and low frequencies, the frequency dependence of |Z| disappears. At the highest frequencies, the electrolytic resistance controls the impedance, and log (Ru) can be determined from the horizontal level at the highest frequency. Alternatively, polarization resistance contributes at the lowest frequencies, and log (Rp + Ru) can be read from the low frequency horizontal portion. Fig. 4. (b) shows circuit behavior representative of a capacitor at frequencies above 1.0 Hz and of a resistor at frequencies below 10K Hz. The plot of impedance (triangle) versus frequency has a breakpoint, which corresponds to the characteristic frequency w= 1/RsCdl or characteristic time constant T= 1/w = 0.05s of the system. The Bode phase plot (square) shows that the phase angle changes from 40° at high frequency to -80° at low frequency. Fig. 4. (b) indicates that the annealing the sample causes an increase of the maximum degree of the phase angle, which confirms the data recorded in Fig. 3.

3.4 Mechanical Testing

The HV0.025 hardness values calculated for annealed and rolled samples are given in Table 5. The hardness is decreased after annealing which can be attributed to the changes in crystallite size during annealing process [34].

Fig. 6. depicts a comparison of all the results obtained from tensile testing of these samples. The results for rolled samples in rolling and transverse directions indicated that the values of stress and strain were roughly equivalent, indicating isotropic mechanical property behavior. The difference between the samples' rolling and transverse strengths can be attributed to the material's microstructure. In the rolling direction, sample strength is greater than in the transverse direction [35, 36]. In addition, the tensile strength of the rolled sample is greater than that of the annealed sample due to the development of fiber texture along the direction of rolling during cold rolling, which results in an inevitable reduction in ductility. Low ductility of rolled samples is primarily due to residual stress, which is removed during the annealing process, thereby improving ductility at the expense of a relatively lower strength for annealed samples. This behavior can be explained by the presence of residual stresses that would be eliminated by annealing [37]. The improved ductility of the samples after annealing can also be attributed to the increased crystallite size. This modification of crystallite size decreases the density of crystal defects and, as a result, the amount of energy required for the movement of dislocations, resulting in an increase in elongation and, depending on the heat treatment temperature, a decrease in strength [35, 36]. The grain size d has a significant impact on the mechanical properties of alloys, as described by the Hall-Petch equation: [37]

$$\sigma = \sigma_o + \frac{k}{\sqrt{d}} \qquad 4$$

After the elastic region has been traversed, it is evident from Fig. 6 that the stress values fluctuate for all samples. This behavior is attributable to the phenomenon of serrated flow, also known as the "Portevin-Le Chatelier" (PLC) effect [38]. In order for this effect to be visible in a metal's stress-strain diagram, grain size is the most

important factor. The PLC effect will be greater the finer the grain size. According to the results of optical microscopy, the crystallite size of H32-treated AA5083 was smaller than that of untreated AA5083, which may be a major reason for the dominant PLC effect observed for all cases studied in this research, as well as the lower ductility of rolled samples. Taking into account the amplitude of the fluctuations, the PLC effect observed in the stress-strain diagram is of type B band [39]. In addition to grain size, it has been observed that the PLC effect is more pronounced in aluminum alloys due to the presence of alloying elements.

Based on their use in marine structures, these alloys would be subject to the combined action of stresses and medium. Stress corrosion cracking (SCC) analysis is therefore the second and most essential component of mechanical characterization studies. From the Tafel plot and EIS diagrams (as mentioned in the corrosion section), it was determined that annealing at 50°C provides the greatest resistance to corrosion attack. Consequently, samples were annealed at 500°C, and SCC analysis was performed on both annealed and rolled samples at 50°C, and the results were compared. Based on the marine application of these alloys, chloride solution was used to test the samples. In addition, to obtain a clearer picture of the corrosion phenomenon, testing was conducted at elevated temperatures to increase the likelihood of medium attack [38]. In addition, the strain rate was kept very low to increase the likelihood of corrosion attack by the medium.

SCC analysis was carried out using simulated marine environment. The type of SCC test selected for this case is slow strain rate testing (SSRT) with strain rate 7.66e-7 s^{-1} and the temperature was maintained at 50ºC. Samples were tested to break point and UTS and % elongation of the samples were computed for both samples to compare their performance in the given conditions.

Figure 7. depicts the stress strain graph obtained from the SCC test for both annealed and unannealed rolled samples. The stress strain plots revealed the maximum value of stress and elongation in samples prior to specimen fracture in a marine environment. In contrast to the results of tensile testing, where the difference in strength was much more pronounced, the difference in strength is diminished in SCC tests. This is a clear indication that the SCC attack on the unannealed rolled samples was significantly more severe than on the annealed samples. This can be attributed to the presence of higher residual stresses in rolled samples, which increases their susceptibility to corrosion attack and decreases their strength in SCC tests [40]. Residual stresses of a compressive nature have a positive effect on corrosion resistance, whereas tensile residual stresses have a negative effect on the corrosion behavior of materials [40]. In the case of the rolled sample, the plate was produced by cold rolling, which leads to the accumulation of tensile residual stresses that have a negative effect on the corrosion behavior, as evidenced by the SCC test performed on these samples. Numerous studies have demonstrated that alloys with lower strength and greater elongation are more resistant to SCC [41].

Thus, it is clear from mechanical testing performed on the annealed and rolled samples that hardness as well as mechanical strength of the material is decreased a bit with heat treatment of the samples but the improvement in terms of ductility is far more prominent and can be useful depending upon the application. Moreover, in terms of corrosion resistance imparted to the samples after annealing is far more prominent which in turn results in a greater improvement for applications of these alloys involving

cumulative action of stress and corrosion. Therefore, it can be concluded that the resistance of material to stress corrosion cracking attack is greatly increased as a result of annealing.

Table 5. Vickers Hardness Value.

Temperature	Mean Hardness Values ± SD
Cold Rolled	87.5 ± 0.66
Annealed 50°C	81.0 ± 0.74

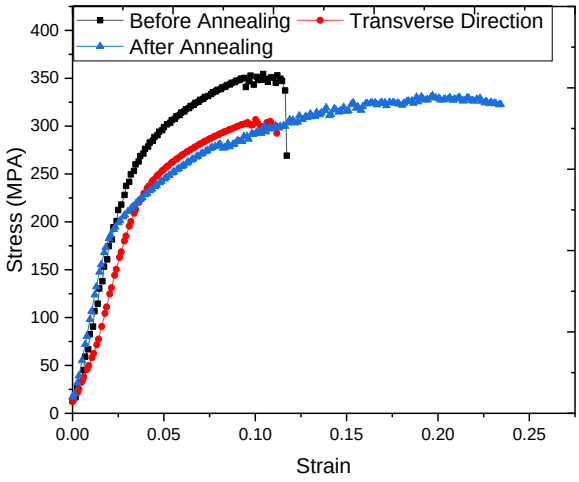

Fig. 6. Tensile testing of cold rolled & 50°C annealed sample.

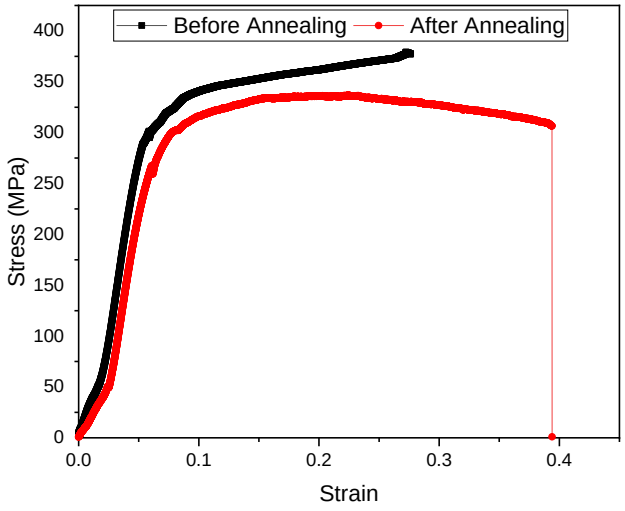

Fig. 7. SCC of cold rolled & 50°C annealed.

3.4 Characterization after Corrosion Studies & Mechanical Testing (SEM Analysis)

Figure 8. depicts the corrosion surface morphologies and EDS of the specimens after potentiodynamic polarization studies. The SEM image reveals the presence of a network of tunnels/channels on the surface of the alloy, a phenomenon known as filiform corrosion. Micrographs depict crystallographic pitting corrosion in the absence of second phase particles, demonstrating that the morphological characteristics of the corrosion attack in this alloy do not depend on corrosion induced by second phase particles, but instead rely solely on grain-specific details [42]. After the onset of corrosion, the corrosion pathway in alloy grains takes the shape of channels along a particular crystallographic plane (200). According to reports, crystallographic pitting is initiated by the breakdown of the oxide film on the surface of the alloy [43], and its propagation is related to the arrangement and orientation of the grains [44]. In NaCl solution, the strong oxidizing ions responsible for pitting are oxygen and chloride ions. The EDX of these channels reveals an oxygen and carbon content of approximately 65 percent, indicating the formation of oxide and carbide [45]. The EDX analysis reveals the formation of Al (Mg, Mn, Fe, Si) particles.

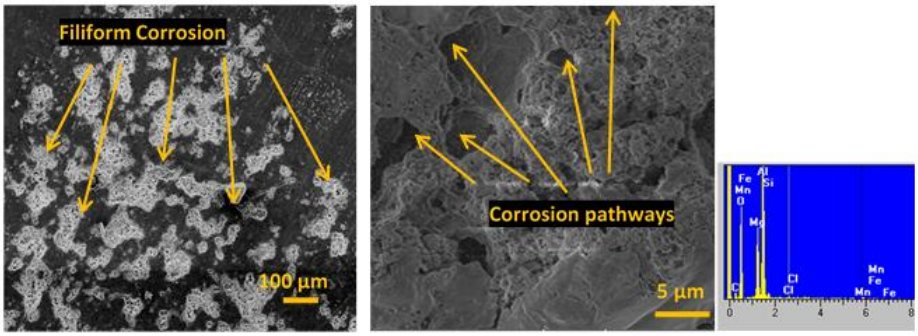

Fig. 8. SEM image after electrochemical testing.

Before and after annealing, scanning electron microscopy (SEM) was performed on the tensile-tested samples. Figure 9. (a) and Figure 9. (b) depict SEM images of an annealed sample and a rolled sample, respectively. The presence of dimples is more pronounced in annealed samples, whereas rock candy morphology with dimples can be observed in rolled samples, indicating that rolled AA5083 has lower ductility. Although there is a combination of ductile and brittle signatures on the fractography of both samples, which can be linked to smaller crystallite size, the ductility is more prominent in the annealed sample than in the rolled sample, as shown by the SEM figures.

Fig. 10. (a) and Fig.10. (b) shows the SEM for rolled and annealed sample after SCC tests were performed using the conditions mentioned. From SEM images, it is clear that the stress strain diagram is depecting the correct behavior in terms of ductility. The signs of brittleness are more dominant in rolled sample as can be seen from fractured sample's fractographs. Energy Dispersive X-Ray Spectroscopy (EDX) was also done for elemental analysis of surfaces of both samples to see whether the failure was solely due to tensile limit or because of the attack of medium (elements in EDX indicate this). Fig. 11. (a) and Fig. 11. (b) shows the EDX obtained for rolled and annelaed samples respectively. The elemental analysis clearly reveal the effect of

medium in the form of presence of sodium, chlorine and other salts. Therefore, it is clear that the environmental solution did have an effect on the performance of material in terms of its strength.

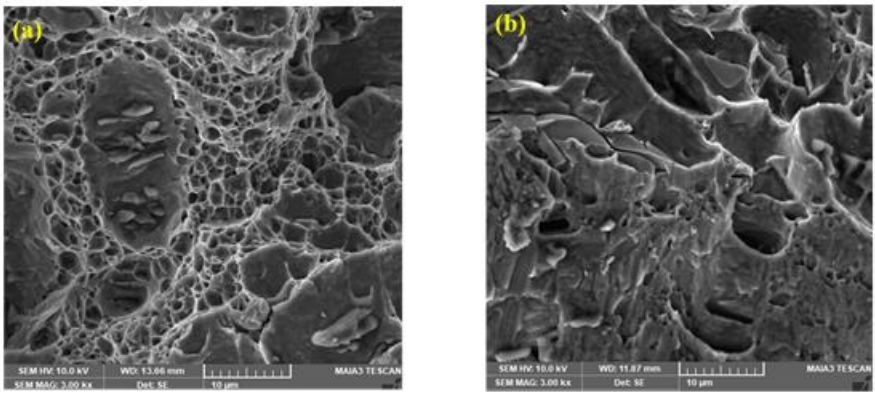

Fig. 9. SEM microstructures of fractured samples after tensile testing of rolled & 50 °C annealed.

One interesting thing observed in the SEM analysis for SCC annealed sample is shown in Fig. 12. As mentioned in the corrosion part these are the inter-metallics which precipitated out. The EDX analysis of the fractured sample shows the main intermetallics which are present in these alloys are iron rich or magnesium rich. As magnesium precipitates require temperature above 65 °C, therefore the intermetallics observed in this case is only iron rich. The formation of intermetallics can become a cause for increased corrosion and thus higher SCC and as a result, lower strength of materials.

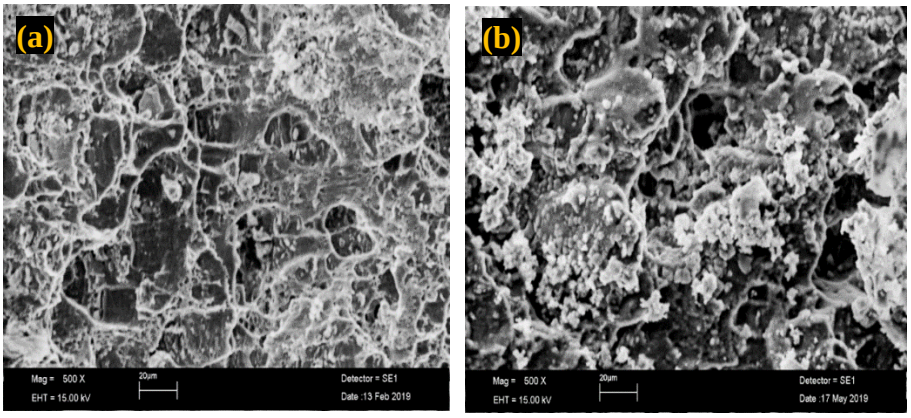

Fig. 10. SEM of rolled & 50°C annealed after SCC testing.

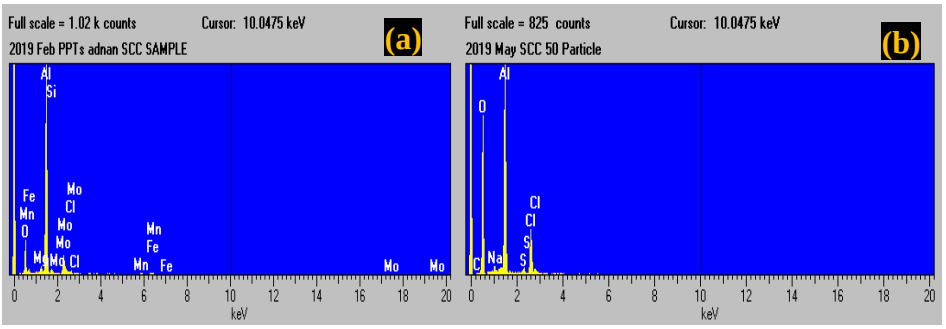

Fig. 11. EDX of rolled & 50°C annealed after SCC testing.

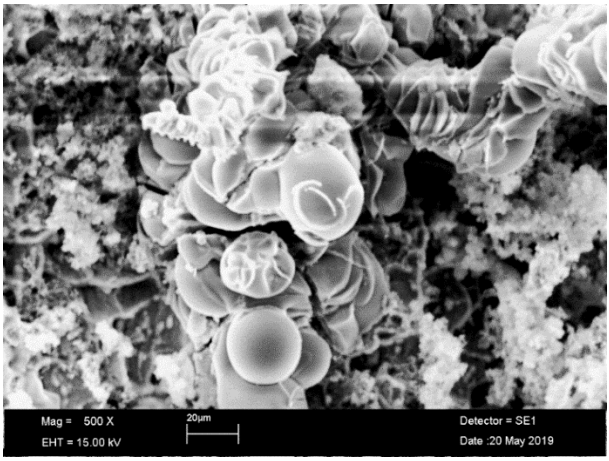

Fig. 12. SEM analysis for SCC annealed sample.

Conclusion

The conclusions acquired are as follows:

1. The heat treatment results in an increase in the size of the crystallites, followed by a reduction in the lattice parameter.
2. Potentiodynamics results show that the corrosion rate decreases after annealing. The electrochemical impedance increases twice by heat treatment compared to the cold-rolled sample, indicating that the corrosion resistance of AA5083 alloy is suitable at 50°C annealing. This improvement in corrosion properties could be due to the removal of residual stresses by annealing, which were produced during cold rolling.
3. Mechanical testing results show that annealing enhanced the ductility of the material. Moreover, considering the application of these alloys in marine environment, results of SCC showed that under combined action of stresses and corrosive environment (simulated water conditions), annealing at 50°C for 30 min have also improved the strength of this alloy in corrosive conditions due to finer crystallite size produced during annealing.

References

[1] Robert J. Mills, Brian Y. Lattimer, Scott W. Case, Adrian P. Mouritz: Corrosion Science 143 (2018) 1-9

[2] F.Gui: Novel corrosion schemes for the aerospace industry, Metals and Surface Engineering (2009) 248-265

[3] H.M.M.A. Rashed, A.K.M. Bazlur Rashid: Comprehensive Materials Finishing, Elsevier, (2017) 337-371

[4] V. N. Gaitonde et al: Journal of Minerals and Materials Characterization and Engineering, 11 (2012) 695-703

[5] J. Kerry: Packaging Technology, Woodhead Publishing, (2012) 163-177

[6] J.R. Davis: Corrosion of Aluminum and Aluminum Alloys, ASM International (1999)

[7] E.L. Huskins, B. Cao, K.T. Ramesh: Materials Science and Engineering A, 527(6): (2010) 1292-1298

[8] J. R. Davis and Associates: ASM Specialty Handbook: Aluminum and Aluminum Alloys ASM International, Materials Park, Ohio, 1994

[9] F.S. Bovard: D.A. Shifler (Ed.), ECS Joint International Meeting, (2004) 232–243.

[10] J.L. Searles, P.I. Gouma, and R.G. Buchheit: Metall. Mater. Trans. A 32 (2001) 2859

[11] R. Goswami, et al: Mater. Sci. Eng., 527A (2010) 1089–1095

[12] Ove Nese, Corrosion properties of AA5083 and AA6082 in seawater - effect of temperature, pH and potential (2016)

[13] Petru Moldovan, Carmen Nicoleta Stanica, Gilbert Ciobanu, Ionel Ungureanu, George Manuel Iorga, Mihai Buţu: I U.P.B. Sci. Bull., Series B, Vol. 76 (3): (2014) 169-180

[14] Zhang, R., Steiner, M.A., Agnew, S.R. et al.: Sci Rep. 7 (2017) 2961

[15] Kiryl Yasaka, M.L. Zheludkevich, Sviatlana V. Lamak, Mario G S Ferreira: Electrochimica Acta 52(27): (2007) 7651-7659

[16] S.O. Adeosun, O.I. Sekunowo, S.A. Balogun, and V.D. Obiekea: Int. J. Corros., 2012, 2012, p 1–9

[17] In et al.: Materials Science and Technology 27 (4): (2011) 789-792

[18] Aline Chemin, Denys Marques et al.: Materials and Design 53 (2014) 118-123

[19] Hosni Ezuber, A. El-Houd, F. El-Shawesh: Materials and Design 29(4): (2008) 801-805

[20] D. Singh et al.: International Journal of Minerals, Metallurgy and Materials 20 (8): (2013) 759

[21] Wang Jinlian, Xu Jun, Pan Feng: Results in Physics 10 (2018) 476-480

[22] P Nageswara Rao,D Singh &R Jayaganthan: Materials Science & Technology 29 (2013) 76-82

[23] Cui Chang-hua, Gao Kun-yuan, Nie Zuo-ren, Wen Sheng-ping, Huang Hui: Corrosion & Protection 32 (2): (2011) 94 - 98

[24] Chun-Hung Yen, Chih-Ting Wu, Yen-Hao Chen, Sheng-Long Lee: Journal of Materials Research 31(08): (2016) 1163-1170

[25] Miljana Popovi, Endre Romhanji: Journal of Materials Processing Technology 125-126: (2002) 275-280

[26] J. Gilbert Kaufman, Introduction to Aluminum Alloys and Tempers, ASM International, (2000) 39-76

[27] Chuanjun Huang et al: 2017 IOP Conf. Ser.: Mater. Sci. Eng. 279 01(2002)

[28] Snopiński P, Tański T, Gołombek K, Rusz S, Hilser O, Donič T, Nuckowski PM, Benedyk M.: Materials 13 (2): (2020) 301
[29] Kalemba-Rec, M. Wróbel and M. Kopyściańsk: Acta Physica Polonica A 130 (2016) 996-999
[30] Masahiko Morinaga: A Quantum Approach to Alloy Design (2019) 221-260
[31] Adriana Valerio, Sergio L. Morelhao: Materials Science, 1(2019)
[32] Malayathodi, Rijesh & Sreekanth, M.S. & Deepak, A. & Dev, K. & Surendranathan, A.O.: International Journal of Mechanical Engineering and Technology, 9 (2018) 646-652.
[33] K. Mallaiya, R. Subramaniam, S.S. Srikandan, S. Gowri, N. Rajasekaran, A. Selvaraj: Electrochim Acta 56 (2011) 3857–3863.
[34] Wang Jinlian, Xu Jun, Pan Feng: Results in Physics, 10 (2018) 476-480.
[35] Juliana de Paula Martinsa, André Luis Moreira de Carvalhob, Angelo Fernando Padilhac: Materials Research, 15(2012) 97-102.
[36] Zainuddin Sajuri, Nor Fazilah Mohamad Selamat, Amir Hossein Baghdadi, Armin Rajabi, Mohd Zaidi Omar, Amir Hossein Kokabi and Junaidi Syarif: Metals, 10(2020) 70.
[37] Naik, S.N., Walley, S.M.: J Mater Sci, 55 (2020) 2661–2681.
[38] D. A. Zhemchuzhnikova, Mikhail Lebyodkin, Tatiana Lebedkina, R. O. Kaibyshev: A, Elsevier, 639 (2015) 37-41.
[39] Ni Tian, Guangdong Wang, Yiran Zhou, Kun Liu, Gang Zhao & Liang Zuo: Materials, 11(2018) 1533.
[40] M. N. James: Engineering Failure Analysis, 18 (2011) 1909-1920.
[41] Zhu, Z., Jiang, X., Wei, G. et al.: Acta Metallurgica Sinica (English Letters), 33 (2020) 1369–1378.
[42] U. Donatus1, G. E. Thompson, J. A. Omotoyinbo, K. K. Alaneme, S. Aribo, O. G. Agbabiaka: Trans. Nonferrous Met. Soc. China, 27 (2017) 55-62.
[43] Xinxin Zhang, Xiaorong Zhou, Teruo Hashimoto, Bing Liu: Materials Characterization, 130 (2017) 230–236.
[44] Newman R.: Journal of Corrosion Science, 37 (1995) 527-533.
[45] Cai D, Han S, Zheng S, Luo Z, Zhang Y, Wang K: Journal of Materials Processing Technology, 255 (2010) 530-535.